

1

2 **Investigating the role of F-actin in human immunodeficiency virus assembly by**
3 **live-cell microscopy**

4 Sheikh Abdul Rahman^{1*}, Peter Koch¹, Julian Weichsel²⁺, William J. Godinez³, Ulrich
5 Schwarz², Karl Rohr³, Don C. Lamb⁴, Hans-Georg Kräusslich¹ and Barbara Müller^{1#}

6 ¹Department of Infectious Diseases, Virology, University Hospital Heidelberg,
7 Heidelberg, Germany. ²BIOQUANT, University of Heidelberg, Heidelberg,
8 Germany. ³BIOQUANT, IPMB, University of Heidelberg and DKFZ, Heidelberg,
9 Germany. ⁴Department of Chemistry and Biochemistry, Ludwig-Maximilians-University,
10 Munich, Germany.

11 Present address: ^{*}HIV Drug Resistance Program, National Cancer Institute, Frederick,
12 USA; ⁺Department of Chemistry, University of California at Berkeley, USA.

13

14 **#Address correspondence to**

15 Barbara Müller
16 Department of Infectious Diseases, Virology
17 Universitätsklinikum Heidelberg
18 Im Neuenheimer Feld 324
19 D-69120 Heidelberg
20 Germany
21 Phone: +49-6221-561325
22 Barbara_Mueller@med.uni-heidelberg.de

23

24

25 Running title: Live imaging of F-actin at HIV-1 budding sites

26

27 **Abstract**

28 Human immunodeficiency virus (HIV-1) particles assemble at the plasma membrane,
29 which is lined by a dense network of filamentous actin (F-actin). High amounts of actin
30 have been detected in HIV-1 virions, proposed to be incorporated by interaction with the
31 nucleocapsid domain of the viral polyprotein Gag. Studies addressing the role of F-actin
32 in HIV-1 particle formation using F-actin interfering drugs did not yield consistent results.
33 Filamentous structures pointing towards nascent HIV-1 budding sites, detected by cryo-
34 electron tomography and atomic force microscopy, prompted us to revisit the role of F-
35 actin in HIV-1 assembly by live-cell microscopy.

36 HeLa cells co-expressing HIV-1 carrying fluorescently labeled Gag and a labeled F-actin
37 binding peptide were imaged by live-cell total internal reflection microscopy (TIR-FM).
38 Computational analysis of image series did not reveal characteristic patterns of F-actin
39 in the vicinity of viral budding sites. Furthermore, no transient recruitment of F-actin
40 during bud formation was detected by monitoring fluorescence intensity changes at
41 nascent HIV-1 assembly sites. The chosen approach allowed us to measure the effect of
42 F-actin interfering drugs on the assembly of individual virions in parallel to monitoring
43 changes in the F-actin network of the respective cell. Treatment of cells with latrunculin
44 did not affect efficiency and dynamics of Gag assembly under conditions resulting in
45 disruption of F-actin filaments. Normal assembly rates were also observed upon
46 transient stabilization of F-actin by short-term treatment with jasplakinolide. Taken
47 together, these findings indicate that actin filament dynamics are dispensable for HIV-1
48 Gag assembly at the plasma membrane of HeLa cells.

49 **Importance**

50 HIV-1 particles assemble at the plasma membrane of virus producing cells. This
51 membrane is lined by a dense network of actin filaments that might either present a
52 physical obstacle for the formation of virus particles, or generate force promoting the
53 assembly process. Drug-mediated interference with the actin cytoskeleton showed
54 different results on formation of retroviral particles in different studies, likely due to
55 general effects on the cell upon prolonged drug treatment. Here we characterized the
56 effect of actin-interfering compounds on the HIV-1 assembly process by direct
57 observation of virus formation in live cells, which allowed us to measure assembly rate
58 constants directly upon drug addition. Virus assembly proceeded with normal rates when
59 actin filaments were either disrupted or stabilized. Taken together with the absence of
60 characteristic actin filament patterns at viral budding sites in our analyses, this indicates
61 that the actin network is dispensable for HIV-1 assembly.

62

63 **Introduction**

64 Human immunodeficiency virus (HIV-1) particles are released from a virus producing cell
65 through the formation of spherical, lipid enveloped virus buds bulging from the plasma
66 membrane; constriction of the bud neck finally culminates in abscission of the virus
67 envelope from the host cell membrane (1). Changes in membrane curvature
68 accompanying bud formation are believed to be induced, at least in part, by cooperation
69 between the viral polyprotein Gag, assembling into a curved protein lattice at the
70 cytoplasmic face of the membrane, and the cellular endosomal sorting complex required
71 for transport (ESCRT) machinery, which is involved in a number of cellular processes
72 requiring membrane abscission. Additional host cell proteins may, however, be exploited
73 by the virus to promote this process.

74 The plasma membrane is lined with a dense and dynamic network of filamentous actin
75 (F-actin) which generates force for cellular processes involving deformation or
76 reorganization of the membrane (e.g. filopodia formation, membrane ruffling or
77 endocytosis, reviewed in (2, 3)). Subversion of the actin cytoskeleton for a variety of
78 replication steps, including particle assembly and release, has been reported for
79 numerous viruses (reviewed in(4)). It is thus conceivable that HIV-1 reorganizes and
80 employs cortical F-actin to promote virus bud formation. In line with this, incorporation of
81 high amounts of actin into HIV-1 (5-7) and a specific interaction of actin with the
82 nucleocapsid (NC) domain of Gag (8, 9) have been reported. However, while the
83 importance of actin cytoskeleton dynamics for the direct cell-to-cell transmission of HIV-
84 1 through so called virological synapses in tissue culture is undisputed((10, 11),

85 reviewed in (4, 12, 13)), the role of F-actin dynamics in the assembly of the viral
86 structure itself is less clearly defined.

87 On theoretical grounds, both a negative influence of F-actin by obstructing membrane
88 access of virion components and/or membrane deformation during bud formation, as
89 well as a positive contribution of forces generated by actin polymerization to membrane
90 bulging, could be envisioned. Analyses of the effect of F-actin interfering drugs on the
91 efficiency of retroviral particle formation yielded different results. Depending on the drug
92 and experimental condition used, complete abrogation of Gag membrane trafficking
93 (14), partial inhibition of particle formation(10, 15), no effect of an F-actin disrupting drug
94 on particle release (10), and even a moderate increase of particle formation in the case
95 of short term cytochalasin D (cyto D) treatment of equine infectious anemia virus (EIAV)
96 producing cells (16) was reported. This can be explained, at least in part, by a difficulty
97 inherent to the ensemble measurements used to quantitate virus production: using bulk
98 virus release as readout necessitates prolonged drug treatment periods, which may
99 favor pleiotropic effects. Thus, potential direct effects on viral particle formation are not
100 easily discriminated from indirect effects. In contrast, live cell imaging provides not only
101 the opportunity to capture transient, non-synchronized interactions between virus and
102 cellular components, but also allows focusing on single cells or individual events.
103 Furthermore, drug effects can be directly visualized within short time windows.
104 Consequently, parallel imaging of virus assembly and F-actin dynamics before, as well
105 as directly after drug addition should allow discriminating between direct and indirect
106 drug effects.

107 Two findings derived from microscopic analyses of HIV-1 assembly sites prompted us to
108 revisit the question of potential F-actin involvement in HIV-1 Gag assembly by exploiting
109 the strengths of a live-cell microscopy approach. First, Gladnikoff and coworkers (17)
110 analyzed nascent retroviral budding sites at the surface of HIV-1 and murine leukemia
111 virus (MLV) Gag expressing 3T3 and HeLa cells by atomic force microscopy (AFM).
112 These authors observed prominent star-shaped structures with arm lengths of up to 4 μ m
113 centered at a subset of budding sites. The large 'asters' were interpreted as structured
114 F-actin assemblies recruited by retroviral Gag; this interpretation was supported by
115 dependence of aster formation on the presence of the presumed actin-interacting NC
116 domain of Gag (17). Second, a morphological connection between F-actin and nascent
117 HIV-1 assembly sites was also conveyed by cryo-electron tomography (cET) of budding
118 sites at the membrane of HIV-1 Gag or GagPol expressing glioblastoma cells (18).
119 Filamentous actin structures were clearly detectable close to 34 of 39 budding sites
120 analyzed and in some cases appeared to be connected to the rims of the bulging HIV-1
121 Gag layer (18).

122 Results from both studies suggested that a Gag mediated reorganization of F-actin
123 structures at the plasma membrane might promote or facilitate the membrane
124 deformations occurring during HIV-1 assembly. However, cET does not yield any
125 dynamic information and AFM measurements were performed with a low temporal
126 resolution (10 min/frame) compared to the time frame determined for completion of an
127 HIV-1 bud ($t_{1/2} \sim 3$ min,(19)). In contrast, single virus tracing (SVT) provides the
128 opportunity to directly observe both F-actin dynamics as well as HIV-1 particle assembly
129 in live cells with high time resolution for a large number of individual budding sites,
130 thereby allowing detection of rapid and transient changes occurring in an asynchronous

131 manner. Using previously characterized fluorescently labeled HIV-1 derivatives (20, 21)
132 together with a fluorescently labeled F-actin binding peptide (Lifeact; (22)) we have
133 analyzed potential interactions of F-actin and nascent viral budding sites in HeLa cells
134 by SVT. The chosen approach allowed us to study F- actin dynamics at individual HIV-1
135 assembly sites and to investigate the influence of treatment with actin interfering drugs
136 on the kinetics of HIV-1 assembly under defined conditions.

137

138 **Materials and Methods.**

139 *Plasmids*

140 Plasmids pCHIV and pCHIV^{eGFP} have been described previously(21). Plasmid
141 pLifeact.mCherry was kindly provided by Nikolas Herold. It was cloned by exchanging a
142 BamHI/NotI fragment from pLifeact.GFP ((22); a kind gift of Michael Sixt) against the
143 corresponding mCherry encoding fragment from pmCherry-N1 (Clontech).

144

145 *Tissue culture and transfections*

146 HeLa cells were cultured in Dulbecco's modified Eagle's medium (DMEM; Invitrogen),
147 supplemented with 10% fetal calf serum (FCS; Biochrom), penicillin (100 IU/mL),
148 streptomycin (100 µg/mL), 4 mM glutamine and 10 mM HEPES (pH 7.4). For co-
149 transfection, cells were seeded in 8-welled glass bottom chamber slides (LabTek, Nunc)
150 at a density of 1.5×10^4 cells/well and transfected the following day with 400 ng of pCHIV
151 derivatives and 100 ng of pLifeact.mCherry. Transfection was performed using either

152 Fugene6 (Roche) or ExtremeGene9 (Roche) according to the manufacturer's
153 instructions. At 12-20 hours post transfection (h.p.t.), cells were transferred to imaging
154 buffer (25 mM HEPES pH 7.4, 137 mM NaCl, 2.7 mM KCl, 1 mM CaCl₂, 1 mM MgCl₂
155 and 30 mM glucose) and subjected to live cell imaging.

156

157 *Cytotoxicity assay*

158 Jasplakinolide solution (1 mM in DMSO) and latrunculin B (LAT-B) were purchased from
159 Calbiochem; a 2.5 mM stock solution of LAT-B was prepared in 100% DMSO. The
160 minimum non-toxic concentration for each drug was determined using a standard MTS
161 cell proliferation assay. For this, HeLa cells were seeded in a 96-well plate at a density
162 of 0.5×10^4 cells per well and incubated overnight at 37°C, 5% CO₂. On the following
163 day, the indicated concentrations of either LAT-B, jasplakinolide, or the corresponding
164 DMSO concentration as a control, were added to the culture medium and incubation
165 was continued for 2 h at 37°C. Cells were washed with pre-warmed phosphate buffered
166 saline (PBS) and stained for dehydrogenase activity using reagents provided in the
167 CellTiter 96 AQueous One Solution Cell Proliferation Assay (Promega) according to the
168 manufacturer's instructions. Cells were incubated for 5h at 37°C followed by
169 measurement of absorbance at 495 nm.

170

171 *Microscopy and single virus tracking*

172 HeLa cells were transfected and prepared for live cell imaging as described above. Basic
173 microscopy settings have been described elsewhere (21, 23). Briefly, live cell imaging

174 was performed using a highly sensitive TIR-FM setup (Objective type, Visitron Systems)
175 based on a Zeiss Axiovert 200M fluorescence microscope equipped with an alpha plan
176 FLUAR 100x/1.45 oil immersion TIRF objective. A 43 series ion laser (MellesGriot) with
177 frequency range of 457 – 568nm was used for excitation at 488nm (eGFP) and 568nm
178 (mCherry). For dual-color imaging the excitation wavelength was chosen by an acousto-
179 optic tunable filter (VTiVisiTech International Vision Technology for Science assembled
180 by Visitron Systems GmbH) coupled to an optic fibre connected with the laser condenser
181 going through the TIRF objective. The TIRF angle was manually controlled. Image
182 sequences were acquired using Metamorph (Visitron) using a sensitive EM-CCD
183 camera (Cascade II, Roper Scientific, 512x512 pixel).

184

185 *Single virus tracking and data analysis*

186 Changes in Gag.eGFP fluorescence intensity over time were analyzed as a signature for
187 the HIV-1 assembly progress. Individual assembly sites were detected and localized
188 using a probabilistic approach for automated tracking of multiple virus particles
189 introduced in (24). Mean fluorescence intensity at the position of identified particles was
190 computed based on the standard deviation of the 2D Gaussian function (σ_{xy}). Signal
191 intensity was measured within the radius of σ_{xy} . Local background intensity was
192 determined based on an annulus with inner and outer radii of σ_{xy} and $5\sigma_{xy}$, respectively
193 and subtracted from the signal intensity measured within the radius of σ_{xy} . In our
194 previous work, we showed that probabilistic tracking methods outperform deterministic
195 ones and achieve accurate results (24). Our probabilistic approach for virus particle
196 tracking was optimized and extended to improve the performance as well as to

197 automatically detect relevant events in the multi-channel microscopy image data. Briefly,
198 with this approach multiple particles are tracked by solving a sequential estimation
199 problem within a Bayesian framework using a Kalman filter for spatio-temporal filtering.
200 For the dynamical model, we used Gaussian random walk dynamics and for the
201 measurement model the intensity information was directly exploited. The tracking
202 approach takes into account anisotropic uncertainty information based on the underlying
203 probability distributions using the Mahalanobis distance. For preprocessing we used a
204 background subtraction scheme based on the filtered image. In addition, we developed
205 an automatic detection scheme for identifying budding events which exploits the steady
206 increase of the intensity over time using a differential approach.

207 Since the temporal distribution of the occurrences of individual assembly sites was
208 asynchronous, we aligned the intensities of different particles by synchronizing the time
209 of initiation of individual assembly sites as described previously (19). Signals identified
210 as typical HIV-1 assembly sites displayed a characteristic change of fluorescence
211 intensity over time: an exponentially growing phase (phase I) representing the dynamic
212 oligomerization of Gag, a plateau phase (phase II) indicating completion of Gag
213 accumulation. A subsequent phase characterized by a rapid change in instantaneous
214 velocity and fluorescence intensity (phase III) was observed only for a subset of traces.
215 Here, the rate of assembly was calculated from phase I by using a saturating
216 exponential function:

$$217 \quad y = A_I (1 - \exp[-k_I (t - t_0)])$$

218 where A_I is maximum fluorescence intensity, k_I is the rate at which fluorescence intensity
219 increases and t_0 is the initial time of assembly.

220 Semi-automatic quantitation of assembly sites in still images was performed using a
221 previously described spot detection algorithm (25). Calculation of rate constants,
222 statistical analyses and plotting of data for all experiments shown was performed using
223 GraphPadPrism.

224

225 *Analysis of LifeAct fluorescence density and coherency from still images*

226 In order to check if virus budding has any statistically significant local effect on the
227 underlying actin cytoskeleton, visible within the resolution of fluorescence microscopy,
228 we analyzed actin patterns in close proximity around the budding sites using an
229 automated image processing approach. We employed two parameters to quantify
230 changes in actin structures, fluorescence density and coherency. Fluorescence density
231 on F-actin stained images is a direct indicator for the local concentration of F-actin, while
232 the coherency analysis is well suited to classify the quality of actin network structures in
233 cells as previously described (26). Briefly, coherency is a side product of the structure
234 tensor analysis, which extracts the local orientation of structures with respect to the
235 squared gray value gradient within a small region of an image, constrained in this
236 context by a Gaussian filter with a size of 9 pixels and a standard deviation of 3 pixels in
237 each dimension (27). Coherency is defined as the squared relative difference of the two
238 squared gray value gradients parallel and orthogonal to the local orientation, i.e. the two
239 eigenvalues of the structure tensor. Therefore, sharp network structures like actin fibers
240 yield maximum coherency values, while for a homogeneous gray value background or
241 white noise the coherency parameter approaches zero.

242 This analysis has been employed before to extract the filament orientation distribution of
243 actin networks from electron tomography data of fish keratocyte lamellipodia (28). Both
244 fluorescence density and coherency in the red channel were measured within a small
245 neighborhood around the individual budding sites and averaged over the time course of
246 budding. The distributions of these temporal averages from all 215 tracked sites in 8
247 different cells are indicated as 'virus' in Figure 1 B and C. For comparison we performed
248 identical analyses at the same number of random positions, uniformly scattered within
249 the outline of the respective cells (Figure 1 B and C, random). Finally, we determined
250 density and coherency averaging over all pixel positions inside the cell boundaries
251 (Figure 1 B and C, 'total'), resulting in an average number of ~29,000 pixels analyzed per
252 cell. This procedure corresponds to the limit of analyzing a large number ($\gg 29,000$) of
253 uniformly randomly located sites within each cell

254

255 **Results**

256 In order to follow HIV-1 virion assembly by live-cell microscopy, we employed our
257 previously described fluorescently labeled HIV-1 derivative pCHIV^{eGFP} (21), which carries
258 an eGFP moiety between the MA and CA domains of Gag. This derivative is non-
259 replication competent due to the lack of viral long terminal repeat regions, but expresses
260 all HIV-1 proteins except for Nef and produces particles with wild-type morphology and
261 cell entry efficiency when complemented with an equimolar amount of its unlabeled
262 counterpart pCHIV(21). Co-transfection of cells with pCHIV and pCHIV^{eGFP} gives rise to
263 punctate fluorescent assembly sites at the plasma membrane, which correspond mostly
264 to individual virus buds and can be followed by live-cell TIR-FM with time resolution in

265 the range of 1 s/frame (19). This experimental system was previously used to
266 characterize the kinetics of the HIV-1 Gag assembly process (19) and the transient
267 recruitment of a cellular protein associated with the endosomal sorting complex required
268 for transport (ESCRT) to nascent budding sites (29).

269 For parallel visualization of F-actin in live cells we made use of an mCherry-tagged
270 version of Lifeact, a 17 amino acid peptide that binds to filamentous actin structures
271 within live eukaryotic cells without detectable interference with cellular processes (22).
272 HeLa cells were co-transfected with Lifeact.mCherry and an equimolar mixture of pCHIV
273 and pCHIV^{eGFP}. Comparison of the dynamic alterations of Lifeact.mCherry in cells co-
274 expressing HIV-1eGFP and Lifeact.mCherry with that in cells transfected with
275 pLifeact.mCherry alone revealed no notable difference in F-actin dynamics observed at
276 the ventral cell surface (supplemental movies S1, S2 and data not shown). At 12-20
277 h.p.t. individual cells co-expressing mCherry and eGFP, which displayed an early stage
278 of budding site formation (evidenced by diffuse cytoplasmic staining for Gag.eGFP and
279 a very low number of detectable budding sites at the plasma membrane), were selected
280 and subjected to microscopic observation over a period of 1-2h. Numerous individual
281 Gag.eGFP punctae appeared at the plasma membrane and gradually increased in
282 fluorescence intensity over a period of several minutes (supplemental movie S2), in
283 accordance with previous findings (19, 30).

284

285 *F-actin distribution patterns with respect to HIV-1 assembly sites.*

286 Formation of prominent μm -sized F-actin structures at the plasma membrane of virus
287 producing cells and in the vicinity of HIV-1 buds as described in(17) should be
288 detectable by TIR-FM, although the spatial resolution of this technique would not allow
289 capturing of structural details. Computational image analysis was performed to obtain
290 information on a statistically significant number of individual sites (Figure 1).

291 We first analyzed the average spatial distribution of F-actin with respect to HIV-1
292 budding sites using an automated image analysis approach (26, 27). The parameters
293 fluorescence density and fluorescence coherency, respectively, were employed in order
294 to detect characteristic F-actin patterns at all individual HIV-1 assembly sites tracked
295 from 8 individual cells ($n=215$). The density of Lifeact.mCherry fluorescence is
296 considered as a direct indicator for the concentration of F-actin at the position of
297 measurement. In contrast, coherency is a parameter chosen to classify the quality of
298 actin network structures in cells. By definition, it extracts the relative strength of the
299 edges of structures compared to their surroundings; thus, sharp and aligned network
300 structures like actin filaments yield maximum coherency values, while coherency values
301 approach zero for a homogeneous gray background or for random noise.

302 We had earlier tested the sensitivity of this parameter to structural changes using
303 simulated microscopy images based on stochastic realizations of a biophysical filament
304 model as a benchmark (26), demonstrating that coherency measurements are well
305 suited to detect changes in the density, intensity and average fiber length of filamentous
306 networks. In the case of star shaped structures, coherency would detect the peripheral
307 aster region, whereas values at the center point may not be significant due to averaging
308 of gradient orientations. However, based on a published fluorescence microscopy image

309 of typical actin aster shapes(17) we expect that density as our second parameter
310 complements this lack of sensitivity by yielding significantly higher values at the central
311 point of asters compared to their surroundings. Therefore we averaged coherency over
312 an annulus with boundaries at 3 and 7 pixels, respectively, around the tracked virus
313 position, while actin density was measured within a circle with a diameter of 6 pixels
314 around the individual budding sites. Both measures were averaged over the time course
315 of assembly in order to detect correlations in the positions of budding sites and the
316 location of ordered F-actin structures.

317 Figure 1 B and C show the distributions of coherency and density measurements,
318 respectively, for 215 individual assembly sites ('virus'). These data were compared to
319 corresponding data sets obtained for either the same number of random positions,
320 uniformly scattered within the boundaries of the respective cell (Figure 1B and C,
321 'random'), or from averaging over the whole area (~29,000 pixel) of the individual cell
322 (Figure 1B and C, 'total'). This analysis did not reveal significant differences in either F-
323 actin coherency or density for HIV-1 budding sites compared to other sites in the same
324 cell.

325

326 *Investigation of actin dynamics at nascent budding sites.*

327 The image analyses summarized in Figure 1 were generated by averaging over the time
328 course of Gag.eGFP assembly and would thus not detect transiently occurring patterns
329 of co-localization that are only visible for part of the observation period. We therefore
330 inspected image series for transient accumulation of F-actin at nascent viral budding

331 sites. Previous characterization of Gag assembly dynamics had revealed that the initial
332 phase of this process follows a saturating exponential at prototypic budding sites (19,
333 30) and that gradual or transient recruitment of ESCRT-components for time periods of
334 less than one minute during this process can be detected (29, 31). Here, we first
335 measured Gag assembly kinetics during the initial exponential phase as described
336 previously (19) in order to control for a possible influence of Lifeact.mCherry expression
337 on HIV-1 assembly. Analysis of >200 tracks from 12 individual cells yielded an average
338 rate constant of $k = 0.005 \pm 0.0026 \text{ s}^{-1}$ in very good agreement with the rate of $k =$
339 $0.0043 \pm 0.0005 \text{ s}^{-1}$ obtained for HeLa cells expressing HIV-1^{eGFP} alone (19). This result
340 indicates that co-expression of Lifeact.mCherry did not alter the dynamics of the HIV-1
341 assembly process.

342 We then analyzed the Lifeact.mCherry signal recorded over time at the positions where
343 HIV-1 budding site formation was detected in TIR-FM (Figure 2 and supplemental movie
344 S3). Only budding sites which were recorded from the onset of Gag.eGFP detection for
345 at least 250 frames were selected for analysis. Figure 2A shows the averaged HIV-1
346 assembly traces of 58 individual assembly sites from 5 different cells recorded in the
347 eGFP channel. Averaged signals recorded in parallel at the identical positions in the
348 mCherry channel are shown in Figure 2B, while Figure 2C displays averaged traces
349 recorded in the red channel at 58 randomly selected non-assembly sites in the same
350 cells. No gradual increase in the Lifeact.mCherry signal over the course of Gag
351 assembly was detected. However, transient recruitment of F-actin at varying time points
352 with respect to the assembly process would be masked by averaging intensities from
353 numerous individual sites. Thus, we also performed manual frame-by-frame inspection
354 of mCherry signal intensities at computationally tracked individual assembly sites (Figure

355 2D-F). In order to account for potential F-actin bursts occurring at early assembly
356 nucleation sites with a number of Gag.eGFP molecules below the detection limit of our
357 approach (32) we included 150 frames (300s) preceding detectable Gag.eGFP
358 accumulation at the respective site in these analyses. Figure 2D and E show examples
359 for a prototypic assembly site (yellow circles) and a non-assembly site (red circles),
360 recorded in the green channel and red channel, respectively. Figure 2F shows the
361 intensity values recorded at the individual assembly site indicated by the yellow circle in
362 Figure 2D for Gag.eGFP (green line) and Lifeact.mCherry (yellow line). The red line
363 shows the Lifeact.mCherry signal recorded during the same time period at the non-
364 assembly site indicated by the red circle in Figure 2D. Inspecting 200 individual tracks
365 for assembly and non-assembly sites did not reveal any characteristic intensity changes
366 associated with Gag assembly: neither a gradual change of mCherry intensity, nor
367 transient bursts of mCherry differing notably from transient fluctuations of
368 Lifeact.mCherry intensity at random membrane positions were detected at nascent Gag
369 assembly sites. In summary, neither characteristic F-actin distribution patterns in close
370 vicinity of nascent budding sites nor typical transient changes in F-actin distribution over
371 the course of HIV Gag assembly were detected by live-cell imaging under our
372 experimental conditions.

373

374 *Effect of pharmacological interference with actin dynamics on HIV-1 Gag assembly*
375 *kinetics.*

376 Although live-cell imaging did not reveal any apparent differences in spatial or temporal
377 F-actin distribution in the presence of Gag assemblies, these findings did not rule out an

378 influence of F-actin dynamics on assembly kinetics. To address this issue, we made use
379 of the fact that live-cell microscopy offers the unique opportunity to analyze virus
380 assembly upon short-term treatment with F-actin interacting drugs while directly
381 monitoring the effect of the drug on F-actin dynamics. Latrunculin B (LAT-B), which
382 binds and sequesters G-actin monomers and thereby prevents actin polymerization (33,
383 34), and jasplakinolide, whose binding to actin oligomers and F-actin filaments stabilizes
384 multimeric actin structures(33, 35), were employed.

385 In order to define effective drug concentrations with minimal adverse effects,
386 cytotoxicity of LAT-B and jasplakinolide under the conditions used was assessed by a
387 colorimetric cell proliferation assay (Celltiter96AQeous, Promega; data not shown).
388 Based on these control experiments, final concentrations of 300 nM LAT-B and 200 nM
389 jasplakinolide, respectively, were chosen for all experiments. HeLa cells were co-
390 transfected with plasmids expressing Lifeact.mCherry and HIV^{eGFP} and grown in the
391 absence of actin interfering drugs. At 20h.p.t., cells were transferred to imaging buffer
392 and microscopically screened for individual cells representing an early stage of
393 assembly site accumulation. Image acquisition was initiated at a rate of 0.5 frames/s and
394 LAT-B, jasplakinolide or DMSO as control, respectively, was added under continuous
395 microscopic observation.

396 Figure 3A, B and supplemental movie S4 summarize the results obtained for LAT-B.
397 Typically, within 100 frames (200 s) after drug addition filamentous actin structures were
398 disrupted and converted into mobile actin clusters moving along the cell membrane with
399 a velocity of $\sim 2\mu\text{m}/\text{min}$, closely resembling the globular structures detected in
400 *Dictyostelium* cells following short-term LAT-B treatment (36). These structures

401 gradually disappeared over time (Figure 3A, top row and Supplemental movie S4).
402 Parallel observation of the Gag.eGFP signal in the same cell revealed that assembly
403 sites continued to form after the addition of drug over the whole observation period of 1
404 h, although filamentous actin structures were efficiently disrupted (Figure 3A lower row
405 and supplemental movie S4). Furthermore, we analyzed rates of assembly after drug
406 addition. A value of $k = 0.0047 \pm 0.0023 \text{ s}^{-1}$, not significantly different from the value
407 determined in control cells ($0.005 \pm 0.0026 \text{ s}^{-1}$; data not shown), was obtained for 71
408 averaged exponential assembly phases from 5 individual LAT-B treated cells (Figure
409 3B).

410 Analogous live-cell imaging experiments were performed in the presence of 200 nM
411 jasplakinolide. In this case, live imaging of Lifeact.mCherry at high time resolution
412 allowed us to distinguish different stages of the jasplakinolide effect, dependent on the
413 time after drug treatment. Addition of jasplakinolide to the imaging buffer initially resulted
414 in apparent stabilization and thickening of stress fibers (Figure 3C, top row and
415 supplemental movie S5). Approximately 5 min after drug addition, formation of
416 amorphous actin aggregates was observed in the cytoplasm, accompanied by filament
417 disintegration. Within ~15-25 min of treatment, all visible F-actin had collapsed into a
418 large aggregate close to the nucleus and cells started to detach from the chamber slide.
419 This is in accordance with findings reported by Bubb *et al.* (35). Jasplakinolide stabilizes
420 F-actin filaments *in vitro* (37) and in live cells, but it also promotes enhanced actin
421 filament nucleation in cells due to stabilization of actin oligomers. The latter effect
422 ultimately results in sequestration of actin in large amorphous polymers, depleting G-
423 actin from the pool available for filament assembly(35).

424 Based on this observation, we divided our analysis of Gag assembly kinetics and
425 budding site formation into the two phases defined by the parallel analysis of
426 Lifeact.mCherry, revealing differential effects on assembly that correlated with the
427 phenotype of the virus producing cell (Figure 3C and supplemental movie S5). During
428 the phase of apparent actin filament thickening, assembly sites continued to form with
429 an average assembly rate $k = 0.0041 \pm 0.0025 \text{ s}^{-1}$ (Figure 3D), again similar to the rate
430 determined for control cells. However, whereas new budding sites displaying
431 exponential assembly kinetics appeared throughout the observation period for control
432 and LAT-B treated cells, respectively (Figure 4A, top and middle panel), almost no new
433 assembly sites were observed after the first 30 min of jasplakinolide treatment (Figure
434 4A, bottom panel) when most cells had reached the actin aggregation state. Visual
435 analysis of image series from jasplakinolide treated cells confirmed that new assembly
436 sites were not detected in cells in which the actin cytoskeleton had collapsed.

437 In order to unmask potential more subtle effects on assembly rates, we analyzed the
438 distribution of assembly rate constants observed dependent on the time points after
439 jasplakinolide or LAT-B addition. In agreement with our earlier observations (19) a rather
440 broad range of rate constants was determined when comparing individual sites, but this
441 range did not vary depending on the time point after drug addition (Figure 4A). The
442 distribution of rate constants determined for individual exponential assembly phases in
443 jasplakinolide treated cells was similar to that observed in control or LAT-B treated cells,
444 respectively (Figure 4B). We conclude that HIV-1 assembly in jasplakinolide treated cells
445 proceeded with normal rates during the phase of F-actin filament thickening and then
446 ceased completely upon actin network collapse. This was supported by the analysis of
447 cells treated with cucurbitacin E, which has been reported to inhibit F-actin

448 depolymerisation by a different mechanism of action(38). Again, Gag assembly in the
449 early phase of cucurbitacin E treatment proceeded with a similar rate ($k = 0.0054 \pm$
450 0.0028 s^{-1}) as in control cells (Figure 3E, F and supplemental movie S6).

451 These experiments showed that drug-induced interference with the F-actin network did
452 not result in decreased Gag assembly rates. On the other hand, cortical actin could be
453 envisioned as an obstacle for nascent bud formation. Resolution of dense cortical actin
454 networks by latrunculin might then facilitate Gag access to the plasma membrane,
455 leading to increased budding frequency. Visual inspection of image series had indeed
456 suggested an increase in the appearance of new assembly sites upon LAT-B treatment
457 in some cases (see supplemental movie S4). To address this question quantitatively, we
458 analyzed the number of assembly sites detected per cell and the rate of new assembly
459 site formation in individual cells (Figure 5). While the total number of assembly sites
460 detected at the plasma membrane varied considerably between individual cells, neither
461 the average value (Figure 5A) nor the variation between individual cells (Figure 5B)
462 differed significantly between LAT-B treated and control cells, respectively.

463 Similar results were obtained when comparing the rate of assembly site initiation
464 measured in live-cell experiments. This rate was assessed either through accumulation
465 of assembly sites over time (Figure 5C) or through calculating the average interval
466 between consecutive detections of individual assembly sites (Figure 5D). In both cases
467 we observed variation between individual cells under the same experimental conditions,
468 but the evaluations did not reveal any clear difference between control and LAT-B
469 treated cells. In accordance with the data shown in Figure 4, accumulation of new
470 assembly sites in jasplakinolide treated cells ceased at ~ 30 min after drug addition

471 (Figure 5C, orange symbols), whereas the interval between consecutive assembly site
472 appearances during the early productive phase was not altered by this compound either
473 (Figure 5D).

474

475 **Discussion**

476 Based on previous reports implicating F-actin in HIV-1 morphogenesis, we have
477 analyzed actin density, actin recruitment and the presence of specific F-actin structures
478 at viral budding sites using live cell TIR-FM. No specific features were detected in the
479 vicinity of nascent assembly sites. Disruption of the F-actin network by treatment with
480 LAT-B affected neither the rate of budding site initiation nor Gag assembly kinetics at
481 individual sites, while the F-actin network was completely disrupted. Furthermore,
482 addition of the F-actin stabilizing compound jasplakinolide also had no significant effect
483 on assembly kinetics and rate of budding site appearance during the early phase when
484 F-actin filament thickening was apparent. Cessation of budding site formation at time
485 points later than 30 min post drug addition in the case of jasplakinolide treatment cannot
486 be attributed to the observed disruption of F-actin filaments at this stage, since particles
487 continued to form with normal efficiency upon filament disruption through LAT-B. We
488 thus consider it likely that termination of assembly in the case of jasplakinolide is due to
489 indirect pleiotropic effects upon complete collapse of the cytoskeleton. Based on these
490 results, we conclude that cortical F-actin is not specifically recruited to HIV-1 budding
491 sites and does not influence the nucleation of assembly sites or the kinetics of assembly
492 in HeLa cells. Our data thus clearly do not support a role of F-actin in HIV-1 Gag
493 membrane transport and assembly, which had been inferred from previous studies.

494 Sasaki and coworkers had reported complete abrogation of membrane localization and
495 particle production upon treatment of T-cells with mycadolide B (14) and a partial block
496 of HIV-1 particle release upon long-term treatment with cytoD (15), respectively.

497 Employment of inhibitory drugs for 3 h (the shortest possible time permitting ensemble
498 measurements) performed by Jolly *et al.* (10) revealed no effect of cytoD and a modest
499 effect of LAT-A on bulk Gag release from T-cells. Whereas these data were taken as
500 evidence for a role of actin dynamics in Gag membrane transport and particle formation,
501 in our view the findings taken together rather argue for indirect effects of long term drug
502 treatment. Although no overt cytotoxicity was observed in these studies, more subtle
503 effects on cell metabolism, protein expression, energy status and/or transport pathways
504 may offer an alternative explanation for the observed moderate reductions in particle
505 formation. Consistent with this interpretation, differential effects depending on the time
506 of drug treatment were observed in the case of infectious equine anemia virus (EIAV):
507 whereas prolonged incubation with cytoD reduced the amount of particles released by
508 ~50%, short-term treatment with either cytoD or LAT-B resulted in enhancement of bulk
509 particle release by 1,5 to 2-fold (16).

510 While live-cell imaging methods are also not without caveats due to the necessity of
511 heterologous labels, specific microscope setups and extensive image analysis, we
512 believe that our study illustrates an important advantage of a live imaging approach. By
513 directly correlating the effect of drug treatment on F-actin to that on particle assembly in
514 the same individual cell, it was possible to dissect differential effects that would be
515 obscured in ensemble measurements. This was particularly apparent in the case of
516 jasplakinolide treatment, where two distinct stages of drug action could be clearly
517 correlated to different effects on Gag assembly. Of note, our bulk toxicity measurements

518 had not shown pronounced cytotoxic effects under conditions at which a large proportion
519 of cells was severely compromised as judged by F-actin live-cell imaging. These
520 observations underline the point that bulk experiments involving the use of chemical
521 compounds with pleiotropic effects have to be interpreted with caution and indicate live-
522 cell imaging methods as an alternative approach.

523 We need to point out, however, that whereas imaging the ventral surface in TIR-FM
524 allows quantitative analyses of new budding site formation and the assembly kinetics of
525 the immature Gag lattice, our experimental system is not well suited for analyses of the
526 subsequent release step. Trapping of viruses in the confined space between cell
527 membrane and cover slip prevents a clear assignment of the actual membrane scission
528 event. Accordingly, our data do not exclude a role of actin in the actual HIV-1 particle
529 release. A contribution of F-actin to virion abscission could explain the modest effects of
530 cytoD and/or latrunculin observed by others on retroviral particle formation in short-time
531 incubation experiments; however, data on HIV-1 suggested a negative effect of F-actin
532 disassembly on release (10), while it was reported to have a positive effect in the case of
533 EIAV (16). Again, ensemble measurements have to be interpreted with caution, since
534 particle formation between individual cells in the same culture is asynchronous; bulk
535 material collected may thus represent a mixture of events initiated before and during the
536 treatment phase. A role of actin in virus release and spread, but not for intracellular
537 transport or assembly of the particle is not without precedent, as actin dynamics is
538 essential for vaccinia virus transmission, while not being relevant for the virus formation
539 process (reviewed in(39)). In the case of measles virus, jasplakinolide treatment was
540 recently reported to specifically affect the step of particle abscission at the plasma
541 membrane (40). Investigating the role of actin dynamics for the HIV-1 membrane

542 abscission event by live-cell imaging, however, is currently prevented by the lack of a
543 suitable microscopic readout to monitor release events. Obviously, our data do not
544 argue against the previously reported role of F-actin dynamics in retroviral cell-cell
545 transmission. Work from several labs has clearly shown that actin plays a role in the
546 formation of virological synapses and for viral transmission through cell surface surfing,
547 nanotubes or cytonemes (reviewed in(13, 41, 42)), while the current study focused on
548 the assembly of individual HIV-1 particles.

549 Previous cET studies had indicated the presence of dense F-actin networks in the
550 vicinity of HIV-1 budding sites and sometimes apparently associated with the budding
551 site (18), and this was confirmed in the accompanying paper of Stauffer *et al.* (43). Our
552 live-cell TIR-FM studies do not argue against such structures, but suggest that the F-
553 actin density does not detectably differ between budding sites and other regions of the
554 plasma membrane. This is in agreement with the observation made by Stauffer *et al.*,
555 that actin was not enriched in HIV-1 particles as compared to the average actin content
556 of the corresponding host cell (43). Furthermore, although we cannot exclude the
557 presence of short, dynamic and possibly also more latrunculin resistant, actin oligomers
558 (44, 45), our studies did not reveal large actin-derived asters at HIV-1 budding sites as
559 had been reported in a previous AFM study (17). This difference cannot be explained at
560 present, but our parallel cETstudy (43) did not detect a difference in actin association
561 when the NC-domain was replaced by a dimerizing leucin zipper, while AFM detection of
562 asters was completely lost in this case (17). Thus the relation between the aster
563 structures uncovered by AFM and the actin networks detected by cET and TIR-FM is
564 currently unclear.

565 In summary, this work, together with the accompanying manuscript by Stauffer *et al.*
566 (43), indicate that F-actin and F-actin dynamics as well as the putative actin-binding NC
567 domain of Gag are dispensable for HIV-1 assembly. Neither actin filaments (disrupted by
568 LAT-B) nor actin treadmilling (disrupted by jasplakinolide) are required for HIV-1 Gag
569 transport, for formation of new budding sites or for assembly of the immature Gag shell.

570

571 **Acknowledgments.** We are indebted to Maria Anders-Össwein and Anke-Mareil Heuser
572 for expert technical assistance. We thank Michael Sixt, Martinsried, for plasmid pGFP-
573 Lifeact and Nikolas Herold for providing pLifeact.mCherry. The distribution of the ImageJ
574 spot detection plug-in by Peter Bankhead, Nikon Imaging Center Heidelberg, is
575 gratefully acknowledged. This work was supported in part by the Deutsche
576 Forschungsgemeinschaft through PhD student fellowships to SAR and PK (GRK1188)
577 and through the collaborative research grant SFB638 (Project A9; HGK). BM and HGK
578 are investigators of the CellNetworks Cluster of Excellence (EXC81).

579

580 **References**

581

- 582 1. Sundquist WI, Kräusslich HG. 2012. HIV-1 Assembly, Budding, and Maturation. *Cold Spring*
583 *Harbor perspectives in medicine* 2:a006924.
- 584 2. Stachowiak JC, Brodsky FM, Miller EA. 2013. A cost-benefit analysis of the physical
585 mechanisms of membrane curvature. *Nature cell biology* 15:1019-1027.
- 586 3. Anitei M, Hoflack B. 2012. Bridging membrane and cytoskeleton dynamics in the secretory and
587 endocytic pathways. *Nature cell biology* 14:11-19.
- 588 4. Taylor MP, Koyuncu OO, Enquist LW. 2011. Subversion of the actin cytoskeleton during viral
589 infection. *Nature reviews* 9:427-439.
- 590 5. Chertova E, Chertov O, Coren LV, Roser JD, Trubey CM, Bess JW, Jr., Sowder RC, 2nd, Barsov E,
591 Hood BL, Fisher RJ, Nagashima K, Conrads TP, Veenstra TD, Lifson JD, Ott DE. 2006. Proteomic
592 and biochemical analysis of purified human immunodeficiency virus type 1 produced from
593 infected monocyte-derived macrophages. *Journal of virology* 80:9039-9052.
- 594 6. Ott DE, Coren LV, Johnson DG, Kane BP, Sowder RC, 2nd, Kim YD, Fisher RJ, Zhou XZ, Lu KP,
595 Henderson LE. 2000. Actin-binding cellular proteins inside human immunodeficiency virus type
596 1. *Virology* 266:42-51.
- 597 7. Ott DE, Coren LV, Kane BP, Busch LK, Johnson DG, Sowder RC, 2nd, Chertova EN, Arthur LO,
598 Henderson LE. 1996. Cytoskeletal proteins inside human immunodeficiency virus type 1
599 virions. *Journal of virology* 70:7734-7743.
- 600 8. Liu B, Dai R, Tian CJ, Dawson L, Gorelick R, Yu XF. 1999. Interaction of the human
601 immunodeficiency virus type 1 nucleocapsid with actin. *Journal of virology* 73:2901-2908.
- 602 9. Wilk T, Gowen B, Fuller SD. 1999. Actin associates with the nucleocapsid domain of the human
603 immunodeficiency virus Gag polyprotein. *Journal of virology* 73:1931-1940.
- 604 10. Jolly C, Mitar I, Sattentau QJ. 2007. Requirement for an intact T-cell actin and tubulin
605 cytoskeleton for efficient assembly and spread of human immunodeficiency virus type 1.
606 *Journal of virology* 81:5547-5560.
- 607 11. Jolly C, Sattentau QJ. 2004. Retroviral spread by induction of virological synapses. *Traffic*
608 (Copenhagen, Denmark) 5:643-650.
- 609 12. Stolp B, Fackler OT. 2011. How HIV takes advantage of the cytoskeleton in entry and
610 replication. *Viruses* 3:293-311.
- 611 13. Sattentau QJ. 2010. Cell-to-Cell Spread of Retroviruses. *Viruses* 2:1306-1321.
- 612 14. Sasaki H, Nakamura M, Ohno T, Matsuda Y, Yuda Y, Nonomura Y. 1995. Myosin-actin
613 interaction plays an important role in human immunodeficiency virus type 1 release from host
614 cells. *Proceedings of the National Academy of Sciences of the United States of America*
615 92:2026-2030.
- 616 15. Sasaki H, Ozaki H, Karaki H, Nonomura Y. 2004. Actin filaments play an essential role for
617 transport of nascent HIV-1 proteins in host cells. *Biochemical and biophysical research*
618 *communications* 316:588-593.
- 619 16. Chen C, Weisz OA, Stolz DB, Watkins SC, Montelaro RC. 2004. Differential effects of actin
620 cytoskeleton dynamics on equine infectious anemia virus particle production. *Journal of*
621 *virology* 78:882-891.
- 622 17. Gladnikoff M, Shimoni E, Gov NS, Rousso I. 2009. Retroviral assembly and budding occur
623 through an actin-driven mechanism. *Biophysical journal* 97:2419-2428.

- 624 18. Carlson LA, de Marco A, Oberwinkler H, Habermann A, Briggs JA, Kräusslich HG, Grünewald K.
625 2010. Cryo electron tomography of native HIV-1 budding sites. *PLoS pathogens* 6:e1001173.
- 626 19. Ivanchenko S, Godinez WJ, Lampe M, Kräusslich HG, Eils R, Rohr K, Bräuchle C, Müller B, Lamb
627 DC. 2009. Dynamics of HIV-1 assembly and release. *PLoS pathogens* 5:e1000652.
- 628 20. Müller B, Daecke J, Fackler OT, Dittmar MT, Zentgraf H, Kräusslich HG. 2004. Construction and
629 characterization of a fluorescently labeled infectious human immunodeficiency virus type 1
630 derivative. *Journal of virology* 78:10803-10813.
- 631 21. Lampe M, Briggs JA, Endress T, Glass B, Riegelsberger S, Kräusslich HG, Lamb DC, Bräuchle C,
632 Müller B. 2007. Double-labelled HIV-1 particles for study of virus-cell interaction. *Virology*
633 360:92-104.
- 634 22. Riedl J, Crevenna AH, Kessenbrock K, Yu JH, Neukirchen D, Bista M, Bradke F, Jenne D, Holak
635 TA, Werb Z, Sixt M, Wedlich-Soldner R. 2008. Lifeact: a versatile marker to visualize F-actin.
636 *Nature methods* 5:605-607.
- 637 23. Koch P, Lampe M, Godinez WJ, Müller B, Rohr K, Kräusslich HG, Lehmann MJ. 2009. Visualizing
638 fusion of pseudotyped HIV-1 particles in real time by live cell microscopy. *Retrovirology* 6:84.
- 639 24. Godinez WJ, Lampe M, Worz S, Müller B, Eils R, Rohr K. 2009. Deterministic and probabilistic
640 approaches for tracking virus particles in time-lapse fluorescence microscopy image
641 sequences. *Medical image analysis* 13:325-342.
- 642 25. Abraham L, Bankhead P, Pan X, Engel U, Fackler OT. 2012. HIV-1 Nef limits communication
643 between linker of activated T cells and SLP-76 to reduce formation of SLP-76-signaling
644 microclusters following TCR stimulation. *J Immunol* 189:1898-1910.
- 645 26. Weichsel J, Herold N, Lehmann MJ, Kräusslich HG, Schwarz US. 2010. A quantitative measure
646 for alterations in the actin cytoskeleton investigated with automated high-throughput
647 microscopy. *Cytometry A* 77:52-63.
- 648 27. Jaehne B. 1997. Digital image processing. Springer, Berlin.
- 649 28. Weichsel J, Urban E, Small JV, Schwarz US. 2012. Reconstructing the orientation distribution of
650 actin filaments in the lamellipodium of migrating keratocytes from electron microscopy
651 tomography data. *Cytometry A* 81:496-507.
- 652 29. Baumgärtel V, Ivanchenko S, Dupont A, Sergeev M, Wiseman PW, Kräusslich HG, Bräuchle C,
653 Müller B, Lamb DC. 2011. Live-cell visualization of dynamics of HIV budding site interactions
654 with an ESCRT component. *Nature cell biology* 13:469-474.
- 655 30. Jouvenet N, Bieniasz PD, Simon SM. 2008. Imaging the biogenesis of individual HIV-1 virions in
656 live cells. *Nature* 454:236-240.
- 657 31. Jouvenet N, Zhadina M, Bieniasz PD, Simon SM. 2011. Dynamics of ESCRT protein recruitment
658 during retroviral assembly. *Nature cell biology* 13:394-401.
- 659 32. Jouvenet N, Simon SM, Bieniasz PD. 2009. Imaging the interaction of HIV-1 genomes and Gag
660 during assembly of individual viral particles. *Proceedings of the National Academy of Sciences*
661 of the United States of America 106:19114-19119.
- 662 33. Spector I, Braet F, Shochet NR, Bubb MR. 1999. New anti-actin drugs in the study of the
663 organization and function of the actin cytoskeleton. *Microscopy research and technique* 47:18-
664 37.
- 665 34. Morton WM, Ayscough KR, McLaughlin PJ. 2000. Latrunculin alters the actin-monomer subunit
666 interface to prevent polymerization. *Nature cell biology* 2:376-378.
- 667 35. Bubb MR, Spector I, Beyer BB, Fosen KM. 2000. Effects of jasplakinolide on the kinetics of actin
668 polymerization. An explanation for certain in vivo observations. *The Journal of biological*
669 *chemistry* 275:5163-5170.
- 670 36. Gerisch G, Bretschneider T, Muller-Taubenberger A, Simmeth E, Ecke M, Diez S, Anderson K.
671 2004. Mobile actin clusters and traveling waves in cells recovering from actin
672 depolymerization. *Biophysical journal* 87:3493-3503.

- 673 37. Bubb MR, Senderowicz AM, Sausville EA, Duncan KL, Korn ED. 1994. Jasplakinolide, a cytotoxic
674 natural product, induces actin polymerization and competitively inhibits the binding of
675 phalloidin to F-actin. *The Journal of biological chemistry* 269:14869-14871.
676 38. Sorensen PM, Iacob RE, Fritzsche M, Engen JR, Brieher WM, Charras G, Eggert US. 2012. The
677 natural product cucurbitacin E inhibits depolymerization of actin filaments. *ACS chemical*
678 *biology* 7:1502-1508.
679 39. Smith GL, Murphy BJ, Law M. 2003. Vaccinia virus motility. *Annual review of microbiology*
680 57:323-342.
681 40. Dietzel E, Kolesnikova L, Maisner A. 2013. Actin filaments disruption and stabilization affect
682 measles virus maturation by different mechanisms. *Virology journal* 10:249.
683 41. Mothes W, Sherer NM, Jin J, Zhong P. 2010. Virus cell-to-cell transmission. *Journal of virology*
684 84:8360-8368.
685 42. Fackler OT, Kräusslich HG. 2006. Interactions of human retroviruses with the host cell
686 cytoskeleton. *Current opinion in microbiology* 9:409-415.
687 43. Stauffer S, Rahman SA, De Marco A, Carlson LA, Glass B, Oberwinkler H, Herold N, Briggs JA,
688 Müller B, Grünewald K, Kräusslich HG. The NC domain of Gag is dispensable for actin
689 incorporation into HIV-1 and for association of viral budding sites with cortical F-actin. *J. Virol.*
690 44. Gowrishankar K, Ghosh S, Saha S, C R, Mayor S, Rao M. 2012. Active remodeling of cortical
691 actin regulates spatiotemporal organization of cell surface molecules. *Cell* 149:1353-1367.
692 45. Collins A, Warrington A, Taylor KA, Svitkina T. 2011. Structural organization of the actin
693 cytoskeleton at sites of clathrin-mediated endocytosis. *Current biology : CB* 21:1167-1175.

694

695 **Figure legends**

696 **Figure 1: Analysis of F-actin density and coherency at nascent HIV-1 budding**
697 **sites. (A)** HeLa cells were co-transfected with pCHIV/pCHIV^{eGFP} and pLifeact.mCherry
698 and analyzed by live-cell TIR-FM at 20 h.p.t. as described in materials and methods.
699 The figure shows TIR-FM still images from supplemental movie S2 recorded in the
700 green (left panel) and red (right panel) channel, respectively, at 20 min after initiation of
701 image acquisition. Squares indicate a representative HIV-1 budding site, circles a
702 representative non-budding site. Scale bar represents 10 μ m. **(B, C)** Distribution of F-
703 actin coherency **(B)** and density **(C)** at 215 HIV-1 budding sites ('virus'), 215 randomly
704 selected non-budding sites ('random'), or all pixels within the boundaries of the
705 respective cells ('total'), respectively. HIV budding sites and non-budding sites were
706 identified from recordings in the GFP channel and density and coherency of the

707 corresponding signal in the red channel were determined as described in materials and
708 methods. The box plots illustrate the distribution of data obtained from eight individual
709 cells. Each box is divided at the median value and lower and upper boundaries of the
710 box indicate the 25th and 75th percentiles of the distribution. Whiskers extend to the
711 most extreme data points within 1.5 times the interquartile range (*i.e.* the range between
712 25th and 75th percentile).

713

714 **Figure 2: Live-cell analysis of Lifeact.mCherry intensity changes at HIV-1**

715 **assembly sites.** HeLa cells were co-transfected with pCHIV/pCHIV^{eGFP} and
716 pLifeact.mCherry. At 20 h.p.t., TIR-FM live cell imaging was performed with a resolution
717 of 0.5 frames/s. Individual HIV-1 assembly sites were tracked as described under
718 materials and methods. **(A-C)** Analysis of mean signal intensity changes over time;
719 mean values (lines), SD (gray bars) and exponential fit (white) are shown **(A)** Mean
720 intensities from exponential assembly phases (58 individual HIV-1 assembly sites from 5
721 cells, recorded in 5 independent experiments) are depicted. **(B)** Mean of the
722 corresponding traces recorded in the red channel (Lifeact.mCherry) for all positions
723 analyzed in (A). **(C)** Mean of traces recorded in the red channel at 58 non-assembly
724 sites from the cells analyzed in (A). **(D)** Image from the live-cell analysis of a
725 representative cell (shown in supplemental movie S3). Examples for an individual
726 assembly site (yellow) and a non-assembly site (red), respectively, are indicated by
727 circles. Scale bar represents 10 μ m. **(E)** Images from supplemental movie S3 recorded at
728 the indicated time points (min:sec) in the green and red channels at the assembly site or
729 non-assembly site encircled in (D), respectively. **(F)** Signal intensity changes over time

730 recorded at the individual assembly and non-assembly sites shown in (E) (green,
731 Gag.eGFP at assembly site; yellow, Lifeact.mCherry at assembly site; red,
732 Lifeact.mCherry at non-assembly site).

733

734 **Figure 3: Effect of pharmacological interference with actin dynamics on HIV-1**
735 **assembly kinetics.** HeLa cells were co-transfected with pCHIV/pCHIV^{eGFP} and
736 pLifeact.mCherry. At 20 h.p.t., medium was changed to imaging buffer and TIR-FM
737 imaging in the green channel and red channels was initiated. **(A, B)** Disruption of actin
738 filaments by LAT-B: At t=0, a final concentration of 300 nM LAT-B was added to the
739 imaging buffer and image series were recorded. **(A)** Images from supplemental movie
740 S4 are displayed for t=0 and for the indicated times after drug addition in the red (3A top
741 row) or green channel (3A bottom row), respectively. The scale bar represents 10 μm .
742 **(B)** Average assembly rate determined after LAT-B treatment. 71 individual assembly
743 sites from 5 cells, recorded in 4 independent experiments, were tracked as described in
744 materials and methods. Mean values (black line), SD (gray bars) and a single
745 exponential fit to the average data (white line) are shown. **(C, D)** Transient stabilization
746 of actin filaments by jasplakinolide. At t=0, a final concentration of 200 nM jasplakinolide
747 was added to the imaging buffer and TIR-FM observation was continued. **(C)** Images
748 from supplemental movie S5 recorded directly before, and at the indicated times after
749 drug addition in the red (top row) or green channel (bottom row), respectively. Scale bar
750 represents 10 μm . **(D)** Average assembly rate determined after jasplakinolide treatment.
751 55 individual assembly sites from 5 cells, recorded in 5 independent experiments, were
752 tracked as described in materials and methods. Mean values (black line), SD (gray bars)

753 and a single exponential fit to the average data (white line) are shown. **(E, F)** Transient
754 stabilization of actin filaments by cucurbitacin E. At $t=0$, a final concentration of 200 nM
755 cucurbitacin E (Calbiochem) was added to the imaging buffer and live imaging was
756 continued (supplemental movie S6). **(E)** Frames from supplemental movie S6 recorded
757 at the indicated times after drug addition in the red (top row) or green channel (bottom
758 row), respectively. The scale bar represents 10 μm . **(F)** Average Gag assembly rate in
759 the presence of cucurbitacin E. A total of 63 individual assembly sites from 3 cells,
760 recorded in 3 independent experiments, were tracked as described in materials and
761 methods. Mean values (black line), SD (gray bars) and a single exponential fit to the
762 average (white line) data are shown.

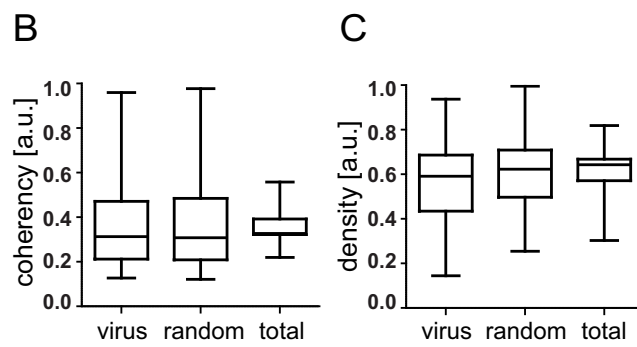
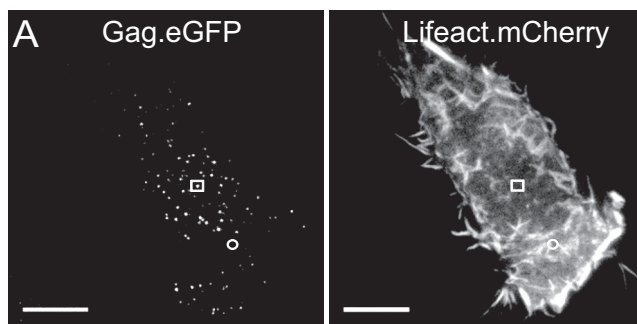
763

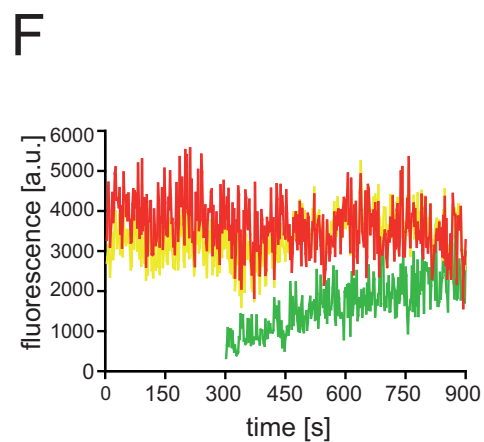
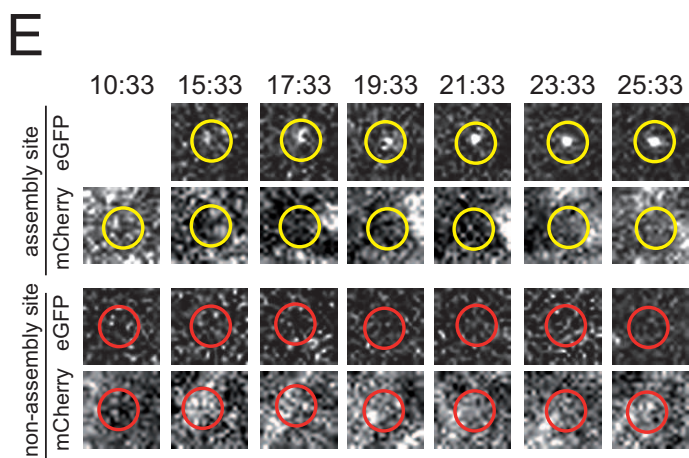
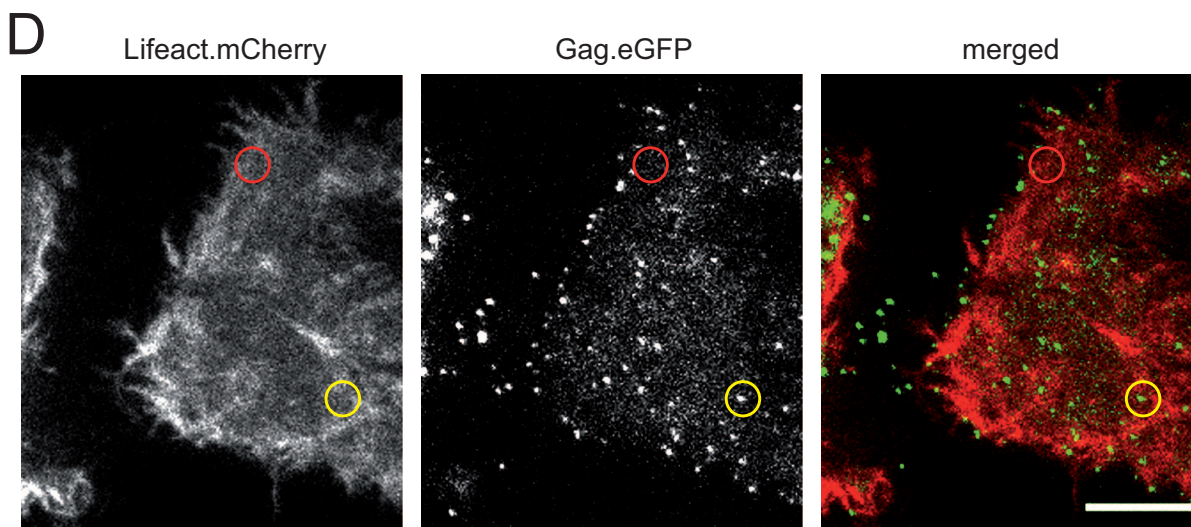
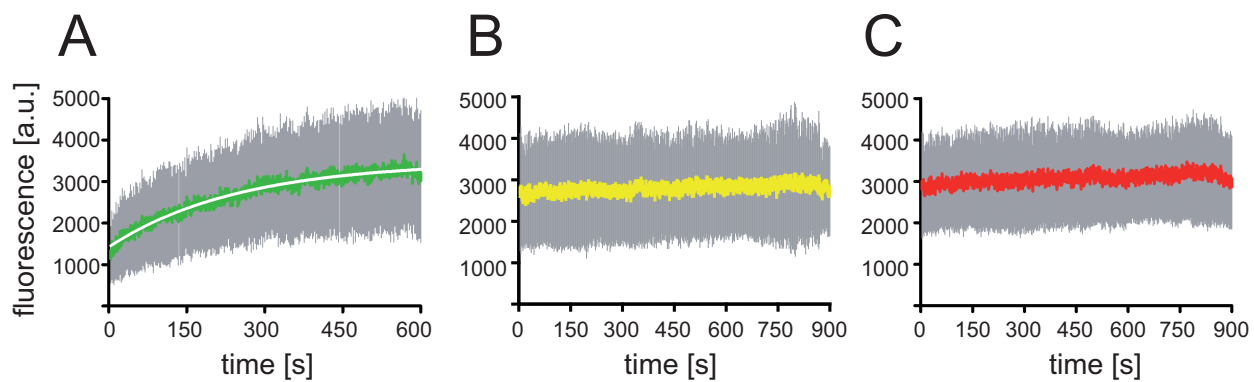
764 **Figure 4. Variation of Gag assembly rates upon F-actin interference.** **(A)** Variation of
765 assembly rates over time. Assembly rate constants from 5 different cells treated with
766 DMSO (top panel; $n=92$ sites recorded in 5 independent experiments), LAT-B (middle
767 panel; $n=106$ sites recorded in 4 independent experiments) or jasplakinolide (bottom
768 panel; $n=66$ sites recorded in 5 independent experiments), respectively were determined
769 from the exponential assembly phase of individual traces and plotted as a function of
770 time of initial detection of the site. $t = 0$ corresponds to the time point of drug addition.
771 **(B)** The histogram illustrates the distribution of number of particles assembling with the
772 respective rates based on the data sets shown in (A).

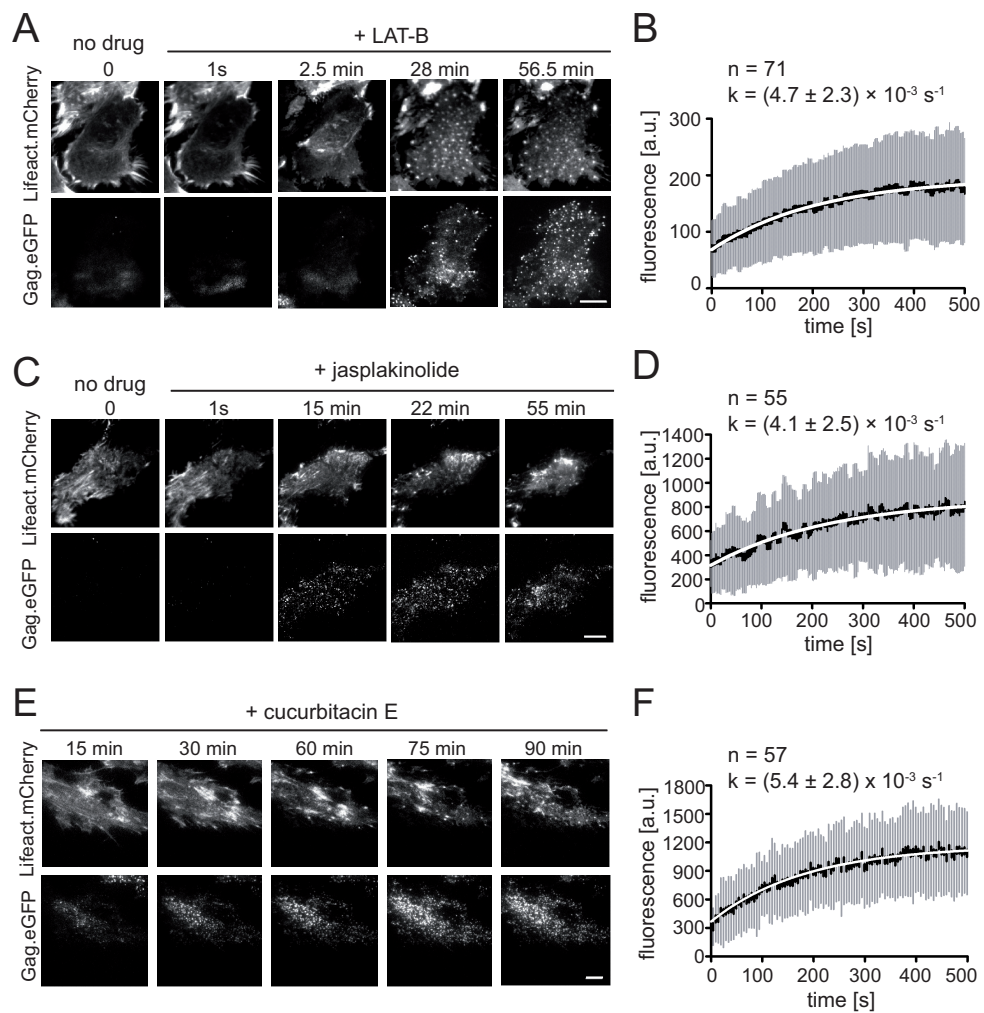
773

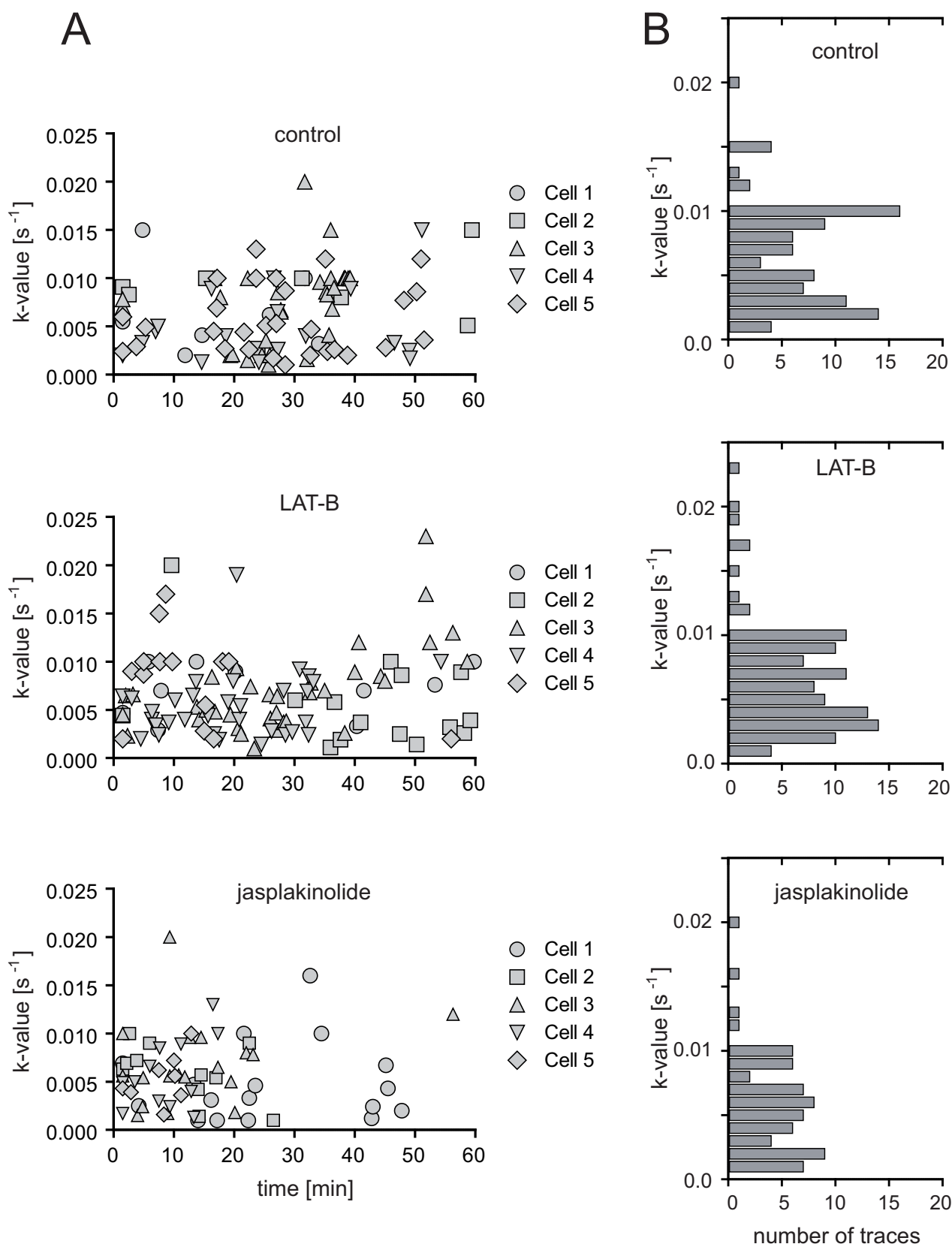
774 **Figure 5: Effect of drug treatment on the appearance of assembly sites at the**
775 **plasma membrane.** **(A, B)** HeLa cells were co-transfected with pCHIV/pCHIV^{eGFP} and

776 pLifeact.mCherry as described in materials and methods. At 12 h.p.t., tissue culture
777 medium was replaced by medium containing 0.1% DMSO (grey bars) or 300 nM LAT-B
778 (black bars), respectively, and incubated for 2 h at 37°C in 5% CO₂. Cells were fixed
779 with 3% PFA and total numbers of budding sites detected per cell were quantitated for n
780 >100 Gag expressing cells per condition by semi-automated analysis of TIR-FM images
781 as described in materials and methods. **(A)** Mean values and SD from three
782 independent experiments. **(B)** Individual cells were stratified according to the numbers of
783 budding sites detected at the membrane. The histogram shows a comparison between
784 DMSO control cells (gray bars) and LAT-B treated cells (black bars). **(C, D)** Formation of
785 new budding sites over time. HeLa cells were co-transfected with pLifeact.mCherry and
786 pCHIV/pCHIV^{eGFP}. At 20 h.p.t., TIR-FM imaging was initiated and DMSO, LAT-B or
787 jasplakinolide, respectively, were added during live cell recording. Automated detection
788 of individual assembly sites appearing after the time point of drug addition (t=0) was
789 performed as described in materials and methods. **(C)** Number of budding sites per cell
790 detected on images recorded at different time points after drug addition. Mean values
791 and standard deviations from five individual cells per condition are shown (green,
792 control; blue, LAT-B; orange, jasplakinolide). **(D)** Time intervals between consecutive
793 initiations of individual assembly events. Average intervals were calculated for five cells
794 (1-5) per condition by linear regression analysis from the time points of appearance for
795 all assembly sites traced for a given cell (n >330 per condition). The plot shows average
796 values and 95% confidence intervals for each individual cell.

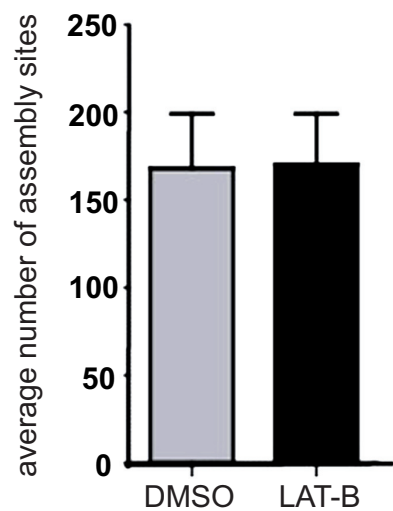




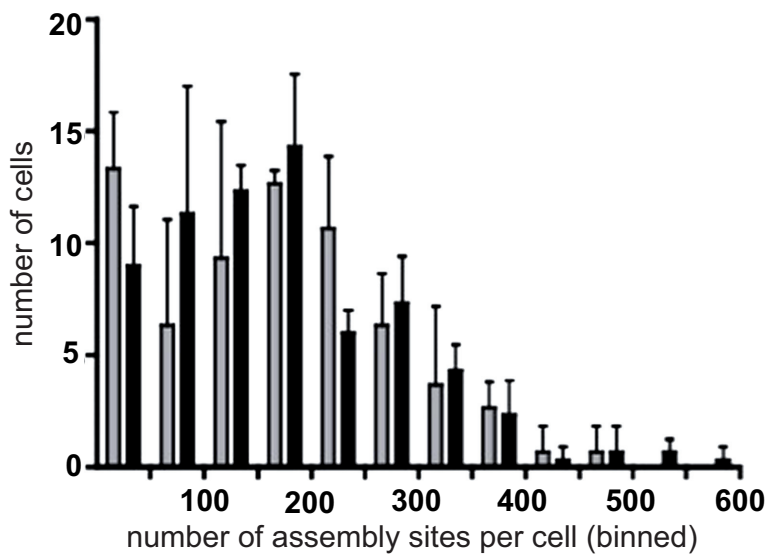




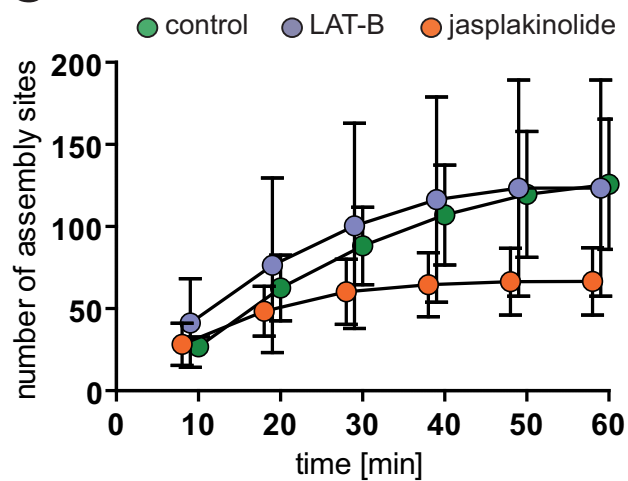
A



B



C



D

